

Modular Synthetic Tissues from 3D-Printed Building Blocks

Alessandro Alcinesio,* Idil Cazimoglu, Gabriella Raye Kimmerly, Vanessa Restrepo Schild, Ravinash Krishna Kumar, and Hagan Bayley*

Biology employs modular organization at every scale: molecular building blocks make up living cells, specialized cells organize within tissues, and collections of tissues constitute organs. 3D-printed networks of picoliter-sized aqueous compartments interconnected by lipid bilayers form a powerful platform for building precisely patterned synthetic tissues. However, this technology has been limited to millimeter-sized networks, with slow fabrication times and lacking flexible design. Here, the authors apply modular design to construct modular synthetic tissues by assembling a wide range of 3D-printed building blocks. They use dedicated modules for storing and releasing reagents, performing logic operations, responding to magnetic fields, and encapsulating living cells. They build centimeter-sized synthetic tissues able to transmit electrical signals through thousands of interconnected compartments. They assemble hybrid tissues composed of both synthetic modules and modules containing living cells. Lastly, by incorporating mutant protein nanopores within the building blocks, they assemble modular synthetic tissues with electrical outputs that are modulated by the integration of chemical inputs.

Modularity is also a widespread design principle in human-made technologies.^[1] A modular approach enables standardization in the design, fabrication, use, and maintenance of devices. Modules are individually designed and fabricated with optimized cost and production time. Different modules are then assembled through standardized interfaces. Novel devices are generated easily and quickly by assembling modules in various architectures, without a need to redesign each part from scratch.^[2] Previously, modular design has been applied to the fabrication of regenerative scaffolds and cell-laden hydrogels using magnetically actuated micro-robots,^[5] DNA-directed self-assembly,^[6] and mechanical interlocking.^[7]

Modular design could also enable a leap forward in the construction of bioinspired devices such as synthetic tissues. Synthetic tissues are cell-free multicom-

1. Introduction

Modularity is the ability to build a system by the assembly of individual independent parts or modules.^[1,2] Each module may have a distinct function, and different modules can work in harmony to produce new, complex functions. Modularity is a major factor in the evolvability and adaptability of living systems, and nature employs it at every level of organization.^[3,4] For example, molecular building blocks make up specialized cells, which in turn form the tissues that comprise organs, which together form entire organisms.

partment systems built from the bottom-up by combining biomolecules such as lipids, proteins, and nucleotides. These cell-free systems can exhibit collective emergent properties resulting from the interaction of hundreds of cell-like units arranged in precise architectures.^[8–10] Importantly, in contrast to most examples in the areas of bioprinting and tissue engineering, synthetic tissues are not designed to exactly replicate the functions of living tissues, but they take inspiration from living tissues to build novel cell-free devices with functions not necessarily found in nature. A robust and versatile platform to build synthetic tissues consists of networks of aqueous droplets interconnected by droplet interface bilayers (DIBs) within an oil^[11,12] or aqueous^[13,14] environment. Within such droplet networks, each droplet acts as a cell-like compartment in which specific chemical cargo and biochemical content can be localized. Furthermore, the lipid bilayers that interconnect adjacent printed compartments can be functionalized by membrane protein pores to control the trafficking of contents among the compartments. Cell-free bioelectronic devices such as batteries^[11] and rectifiers^[15] have been generated from hand-made synthetic tissues. By the 3D-printing of picoliter-sized aqueous droplets in desired architectures, sophisticated synthetic tissues able to transmit electrical signals,^[8,16] undergo macroscopic folding,^[8] and express proteins in response to light^[17] have also been generated.

However, the production of synthetic tissues has so far been limited by the speed of fabrication, the size of the networks that can be generated, and a lack of flexibility in design. The slow manufacturing time of synthetic tissues has resulted from time-consuming droplet-by-droplet 3D-printing, limiting the

A. Alcinesio, I. Cazimoglu, G. R. Kimmerly, V. Restrepo Schild, R. Krishna Kumar, H. Bayley
Department of Chemistry
University of Oxford, Chemistry Research Laboratory
12 Mansfield Road, Oxford OX1 3TA, UK
E-mail: a.alcinesio@gmail.com; hagan.bayley@chem.ox.ac.uk

G. R. Kimmerly
Seattle Children's Research Institute: Building Cure
1920 Terry Ave, Seattle WA 98101, USA

 The ORCID identification number(s) for the author(s) of this article can be found under <https://doi.org/10.1002/adfm.202107773>.

© 2021 The Authors. Advanced Functional Materials published by Wiley-VCH GmbH. This is an open access article under the terms of the Creative Commons Attribution License, which permits use, distribution and reproduction in any medium, provided the original work is properly cited.

DOI: 10.1002/adfm.202107773

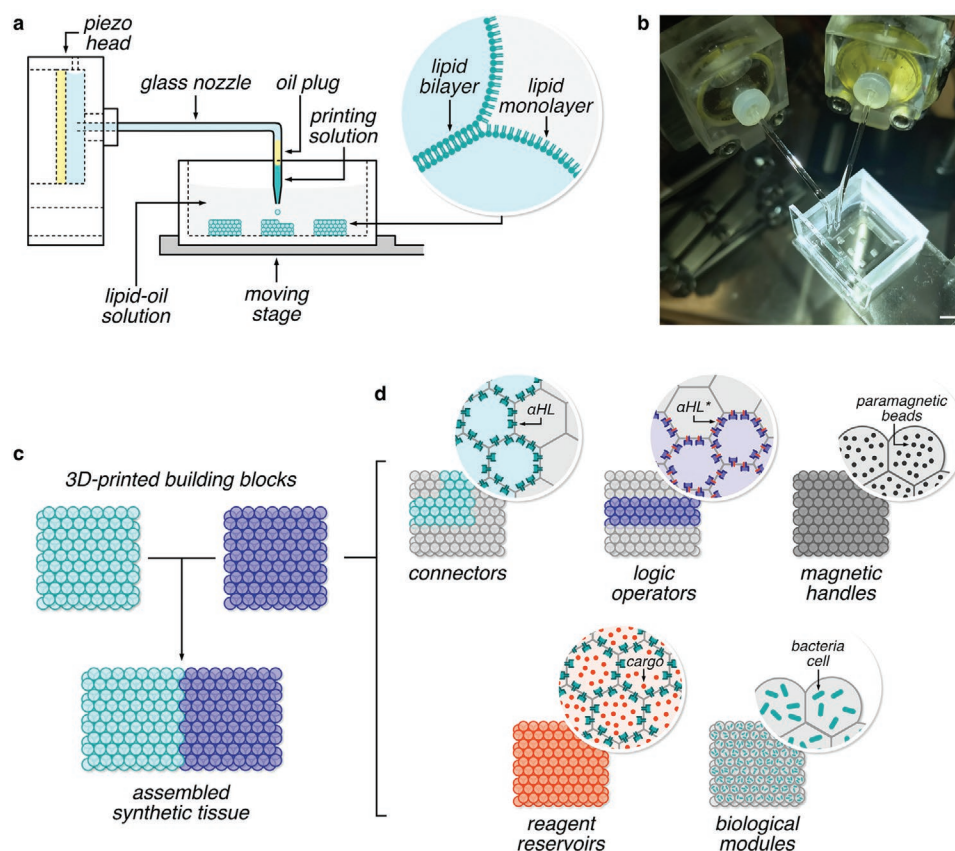


Figure 1. Assembly of modular synthetic tissues from 3D-printed building blocks. a) Diagram of the droplet-on-demand 3D-printer used to generate the building blocks. b) Photograph of the 3D-printer. Scale bar, 5 mm. c) Assembly of a synthetic tissue from two 3D-printed building blocks. d) Overview of the library of modules generated in this work, comprising: conducting connectors produced by patterning droplets containing the pore forming protein α HL, logic operators obtained by incorporating engineered α HL mutants (α HL*) able to respond to environmental signals, magnetic handles with encapsulated paramagnetic beads, reagent reservoirs containing α HL and cargo molecules, and biological modules encapsulating living cells.

networks of compartments to millimeter sizes. Further, the need to redesign and optimize fabrication of synthetic tissues for each new purpose from scratch has limited the rate at which novel applications can be generated.

Here, we demonstrate for the first time the versatile fabrication of modular synthetic tissues with novel functions by assembling a wide range of independently 3D-printed building blocks (Figure 1). Thanks to the modular approach, we can 3D-print building blocks in parallel to increase the fabrication speed and enable scale-up. We assemble independently printed building blocks to generate centimeter-sized networks of thousands of compartments interconnected by lipid bilayers. We interconnect the building blocks by forming lipid bilayers at their contact interfaces, therefore our final assembled synthetic tissues consist in a continuous lattice of lipid-bilayer-interconnected compartments. Our modular approach allows us to assemble synthetic tissues with no restriction on the number of droplet types that can be patterned. Furthermore, building blocks generated under incompatible printing conditions, such as at different temperatures, can also be assembled into heterogeneous synthetic tissues. By this approach, we seamlessly assemble a wide variety of building blocks containing aqueous solutions, molecular cargoes, engineered membrane proteins, paramagnetic particles, hydrogels, and living cells (Figure 1d). By using a diverse

library of building blocks, we generate synthetic tissues that store and release reagents, perform logic operations, respond to magnetic fields, and interact with living cells.

2. Results and Discussion

2.1. Connecting 3D-Printed Building Blocks

We first demonstrated assembly of 3D-printed building blocks into higher order synthetic tissues (Figure 2a). We 3D-printed two building blocks within an oil bath containing 1,2-diphytanoyl-*sn*-glycero-3-phosphocholine (DPhPC), as previously described^[8,16] (Figure 2b, see Experimental Section). Each block consisted of $8 \times 9 \times 5$ ($w \times d \times h$) picoliter-sized aqueous droplets ($\approx 100 \mu\text{m}$ droplet diameter, $\approx 520 \text{ pL}$ droplet volume) interfaced by phospholipid bilayers. We then manually moved the building blocks into contact by using a flat metal spatula (Figure 2b). By using fluorescent dyes with high affinity for lipid bilayers^[18] (Atto550M and Atto647NM) in each of the two building blocks, we demonstrated the formation of lipid bilayers at the interface, as indicated by the co-localization of the fluorescent signals (Figure 2c).

To demonstrate the formation of a functional bilayer interface between the two building blocks, we encapsulated the

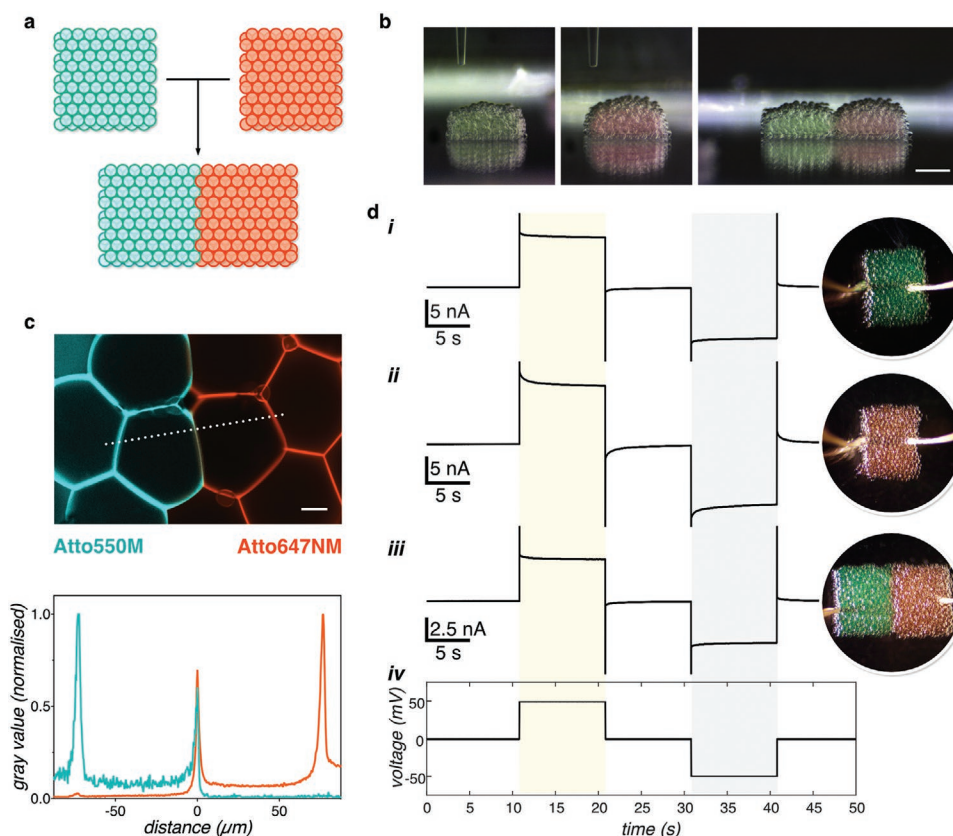


Figure 2. Connecting 3D-printed building blocks. a) Diagram of the assembly of a synthetic tissue from two 3D-printed building blocks. b) Side-view stereomicroscopy images of two 3D-printed building blocks before and after assembly. c) Top, confocal microscopy image of the interface between two assembled building blocks containing fluorescent dyes with high affinity for lipid bilayers. Bottom, line scans of the fluorescence signals along the dotted line in (c), showing the co-localization of the two dyes at the contact interface of the building blocks. d) Recordings of ionic currents flowing through each of the 3D-printed building blocks containing α HL (i and ii), through the assembled synthetic tissue (iii), upon application of the voltage protocol shown in (iv). Stereomicroscopy images of the corresponding synthetic tissues are shown as insets. Scale bars, 500 (b) and 25 μ m (c).

membrane pore-forming protein α -hemolysin (α HL) within the 3D-printed droplets. This pore-forming protein is known to self-assemble into lipid bilayers and allow the transfer of small molecules^[19–22] and transmission of ionic currents^[8,11,16] through lipid-bilayer-interconnected aqueous compartments. We then investigated the electrical properties of the assembled synthetic tissue (Note S1, Supporting Information). At an applied potential $V = +50$ mV, we measured steady-state ionic currents $I_1 = 9.7 \pm 0.1$ nA and $I_2 = 11.5 \pm 0.2$ nA flowing through the individual building blocks before assembly (Figure 2d -i,ii). After assembly, we measured a steady-state ionic current $I_{\text{joined}} = 4.6 \pm 0.1$ nA flowing through the assembled synthetic tissue (Figure 2d -iii), demonstrating that α HL pores had inserted into the lipid bilayers connecting the building blocks (Table S1, Supporting Information).

By applying Ohm's Law, we calculated the effective resistance (i.e., the total observed resistance of the circuit formed by the network of droplets interconnected by α HL-permeabilized lipid bilayers) of each building block, $R_1 = V / I_1 = 5.17 \pm 0.05$ M Ω and $R_2 = V / I_2 = 4.36 \pm 0.08$ M Ω , and the resistance of the assembled synthetic tissue, $R_{\text{joined}} = V / I_{\text{joined}} = 10.84 \pm 0.11$ M Ω . The resistance of the assembled synthetic tissue R_{joined} was higher than the sum of the resistances of its components, $R_1 + R_2 = 9.6 \pm 0.13$ M Ω ($p < 0.001$, unpaired t -test with

Welch's correction). This phenomenon is similar to the electrical contact resistance found in conventional electrical systems based on solid-state conductors, which arises from a reduced true area of contact between different electrical components caused by surface imperfections or oxidation.^[23] In our system, we attributed the increase in resistance to the roll-off of the top edges of the 3D-printed building blocks (Figure 2b). As we observed previously,^[16] a small fraction of droplets located at the top edges of our 3D-printed building blocks roll to the lower droplet layers during printing. This leads to a roll-off of the top edges of the building blocks and consequently to a smaller cross-sectional area of contact between assembled building blocks compared to the cross-sectional area in the middle of each individual building block (Figure 2b). We further confirmed the presence of contact resistance in assembled synthetic tissues by comparing I_{joined} to the steady-state current measured in a 3D-printed synthetic tissue of equal size ($16 \times 9 \times 5$ droplets, $w \times d \times h$, double the size of each building block composed of $8 \times 9 \times 5$ droplets) $I_{\text{double}} = 7.0 \pm 0.1$ pA (Figure S1, Supporting Information). As expected, $I_{\text{double}} > I_{\text{joined}}$, indicating that the effective resistance of two assembled building blocks was higher than the resistance of a synthetic tissue of equal size obtained by direct printing. Despite this effect, our results demonstrate

that a reliable and functional junction could be formed between the two assembled building blocks.

Interestingly, we also observed that conductive synthetic tissues can be cut and then re-assembled, regaining their ability to conduct ionic currents (Figure S2, Supporting Information). This observation opens up to the design of modular systems where modules can be assembled and re-assembled as needed.

2.2. Scaling-Up the Fabrication of Synthetic Tissues

Next, we applied the modular assembly of 3D-printed building blocks to generate centimeter-sized synthetic tissues. We 3D-printed six building blocks composed of $18 \times 12 \times 5$ ($w \times d \times h$) picoliter-sized droplets ($\approx 100 \mu\text{m}$ droplet diameter, $\approx 520 \text{ pL}$ droplet volume) containing αHL . To speed-up the fabrication process, we printed pairs of building blocks in parallel by simultaneous ejection from two printing heads in the same printing container (Figure 3a). Clearly, even greater speeds could be achieved with more than two printing heads. After printing, we joined the six building blocks in a linear fashion (Figure 3b) to obtain a synthetic tissue of $\approx 1.2 \text{ cm}$ in length (Figure 3c) composed of more than 6000 droplets interconnected by αHL -permeabilized lipid bilayers. By applying a potential $V = 100 \text{ mV}$ across the synthetic tissue, we recorded a steady-state ionic current $I_6 = 1.4 \pm 0.1 \text{ nA}$, confirming the structural and functional integrity of the assembled synthetic tissue.

We then studied how the effective resistance R_N of a synthetic tissue composed of N identical building blocks of resistance R_1 varied with N . Based on our observations with two building blocks, we hypothesized that the total effective resistance R_N would be:

$$R_N = NR_1 + (N - 1)R_C \quad (1)$$

where R_C is the contact resistance (Note S1, Supporting Information). To validate this model, we measured the steady-state ionic currents $\{I_1, I_2, \dots, I_6\}$ flowing through $N = \{1, 2, \dots, 6\}$ assembled building blocks (at an applied potential $V = +100 \text{ mV}$, Figure S3 and Table S2, Supporting Information), and calculated the corresponding effective resistances $\{R_1, R_2, \dots, R_6\}$. We estimated the contact resistance R_C from R_1 and R_2 as:

$$R_C = R_2 - 2R_1 \quad (2)$$

and verified that the measured steady-state ionic currents $\{I_1, I_2, \dots, I_6\}$ were in good agreement with the curve:

$$\hat{I}_N = V/R_N = V/[NR_1 + (N - 1)R_C] \quad (3)$$

where \hat{I}_N is the predicted current flowing through a synthetic tissue composed of N assembled building blocks of effective resistance R_1 , under applied voltage V (Figure 3d, green dashed line). Using Equation (3), we can infer that by assembling 500 building blocks, we could form a synthetic tissue of 1 m in length, able to conduct an ionic current of $\approx 10 \text{ pA}$ under applied voltage $V = 100 \text{ mV}$.

2.3. Assembly of Synthetic Tissues by Tiling of Building Blocks

We generated patterned synthetic tissues by the tiling of building blocks. We first 3D-printed two types of building blocks of $14 \times 8 \times 5$ ($w \times d \times h$) droplets, one type containing αHL and the other without αHL . We assembled eight building blocks, four of each type, according to a common basket-weave tiling pattern, in such a way that the building blocks containing αHL formed a conductive cross-shaped pathway spanning the synthetic tissue (Figure 3e). We then measured the steady-state ionic current $I_{\text{tiled},1} = 78 \pm 0.1 \text{ nA}$ flowing through the tiled synthetic tissue and confirmed its structural and functional integrity (Figure 3g; Table S3, Supporting Information). In this way, we demonstrated the formation of patterned synthetic tissues by the tiling of unpatterned building blocks.

We then generated 3D-printed building blocks containing simple patterns and tiled them to generate synthetic tissue with higher order patterns. For example, we printed building blocks of $12 \times 12 \times 5$ droplets ($w \times d \times h$) containing four-droplet-wide L-shaped pathways that contained αHL , surrounded by droplets that did not contain αHL (Figure 3f). We then joined four patterned building blocks to obtain an assembled synthetic tissue containing a sinusoidal conductive pathway. We confirmed the correct functionality of the assembled synthetic tissue by recording a steady-state ionic current $I_{\text{tiled},2} = 3.2 \pm 0.1 \text{ nA}$ through the conductive pathway, while no flow of current was detected outside the pathway (Figure S4 and Table S3, Supporting Information).

2.4. Stacking of Building Blocks by Magnetic Levitation

In order to stack synthetic tissues along the z -direction, we needed to lift building blocks from the printing surface and deposit them on top of other building blocks (Figure 4a). We generated magnetically susceptible building blocks by 3D-printing melted agarose at $\approx 30 \text{ }^\circ\text{C}$ containing paramagnetic beads. After printing, we gelled the agarose at $4 \text{ }^\circ\text{C}$ for 1 h , resulting in building blocks composed of lipid-bilayer-interconnected agarose droplets encapsulating paramagnetic beads (Figure 4b). We then used a neodymium magnet to lift and manipulate the magnetically susceptible building blocks within the oil bath without direct contact (Figure 4c and Video S1, Supporting Information). The use of agarose allowed us to produce an even dispersion of beads within the droplets during printing by increasing the sedimentation time of the beads within the nozzle (Figure 4b). After gelation, the agarose also trapped the beads in place, preventing them from destabilizing the lipid bilayers during magnetic manipulation.

To demonstrate the assembly of a functional synthetic tissue by stacking, we generated three building blocks. Two were not magnetically susceptible and were patterned in such a way to form an assembled synthetic tissue with a pathway of droplets containing αHL interrupted by droplets not containing αHL (Figure 4d,e). Upon application of a voltage, no current was detected (Figure 4h; Table S4, Supporting Information) as expected. The third building block contained a conductive droplet pathway, composed of aqueous droplets with αHL , surrounded by magnetically susceptible droplets, composed of

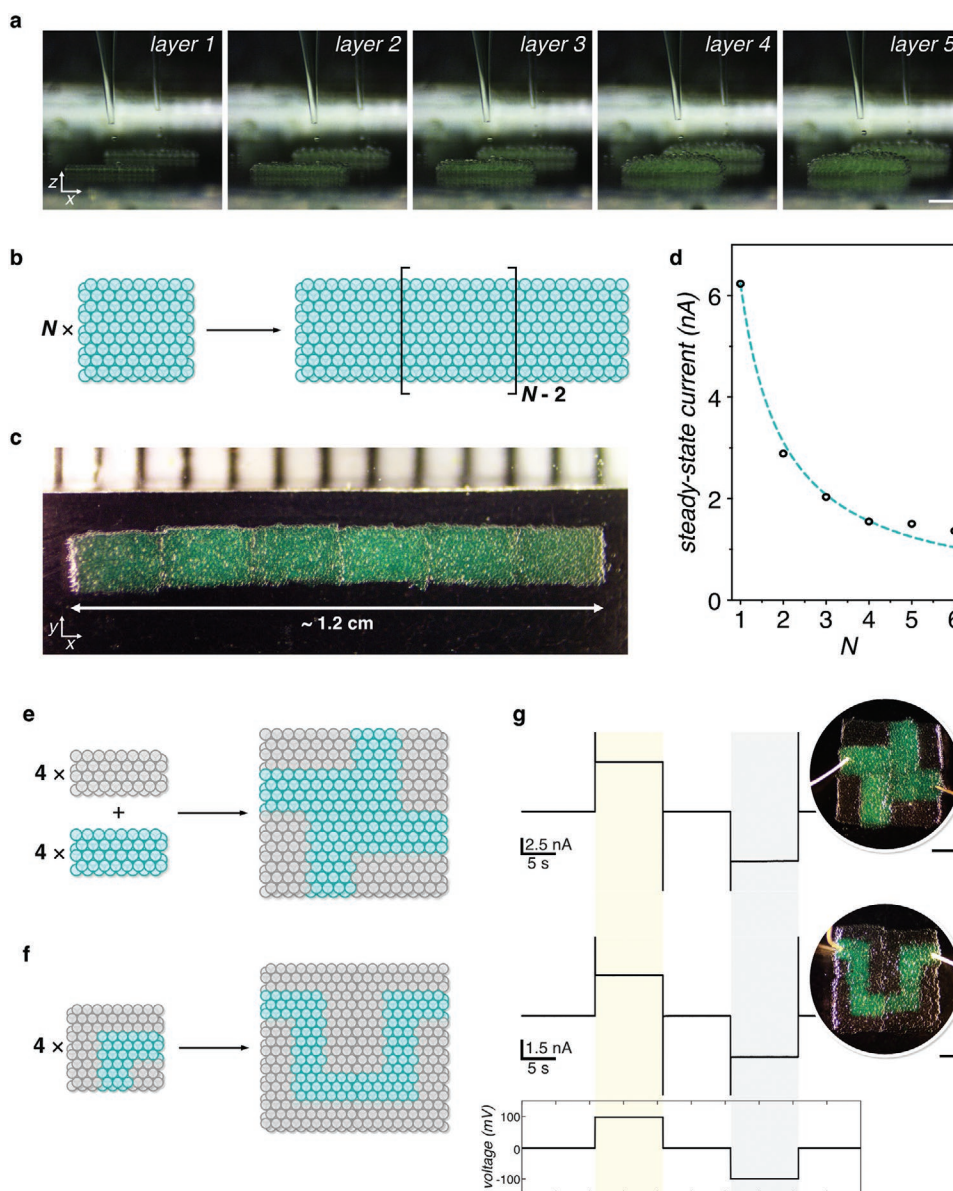


Figure 3. Scaling-up the fabrication of synthetic tissues. a) Side-view stereomicroscopy images showing the parallel printing of two building blocks during deposition of layers 1 to 5. Scale bar, 500 μm . b) Diagram of the assembly of N 3D-printed building blocks into a centimeter-sized synthetic tissue. c) Top-down stereomicroscopy image of a synthetic tissue assembled from six building blocks containing αHL and of ≈ 1.2 cm length. d) Plot of the steady-state ionic currents versus the number of building blocks (N) in the linear constructs (applied voltage $V = +100$ mV, see Figure S3 and Table S2, Supporting Information, for raw data). The decrease in current with N , based on the contact resistance model of Equation (3), is indicated by the dashed green curve. e) Diagram of the assembly of a synthetic tissue from 8 rectangular building blocks by following a tiling pattern. The four teal building blocks contained αHL , while the gray ones didn't. f) Diagram of a synthetic tissue made by assembling building blocks containing a conductive L-shaped pattern (teal, containing αHL). g) Electrical recordings of ionic currents flowing through synthetic tissues assembled as in (e) and (f). Stereomicroscopy images of the corresponding synthetic tissues are shown as insets. Scale bars, 800 (top) and 500 μm (bottom).

gelled agarose with embedded paramagnetic beads. We magnetically levitated and deposited this building block on top of the two previously assembled blocks, to connect the two ends of the interrupted pathway (Figure 4f,g). After inclusion of the magnetically susceptible building block, we measured a steady-state ionic current $I_{\text{stack}} = 690 \pm 20$ pA, upon application of a potential $V = 10$ mV, confirming the functionality of the construct. We also showed that no current flowed through the bilayers separating the droplets with magnetic beads, con-

firmed their integrity (Figure S5 and Table S4, Supporting Information).

2.5. Diffusion of Chemicals in Synthetic and Hybrid Tissues

Next, we investigated the diffusion of chemicals through assembled synthetic tissues. We 3D-printed and assembled two building blocks, one acting as a Ca^{2+} reservoir module, and the

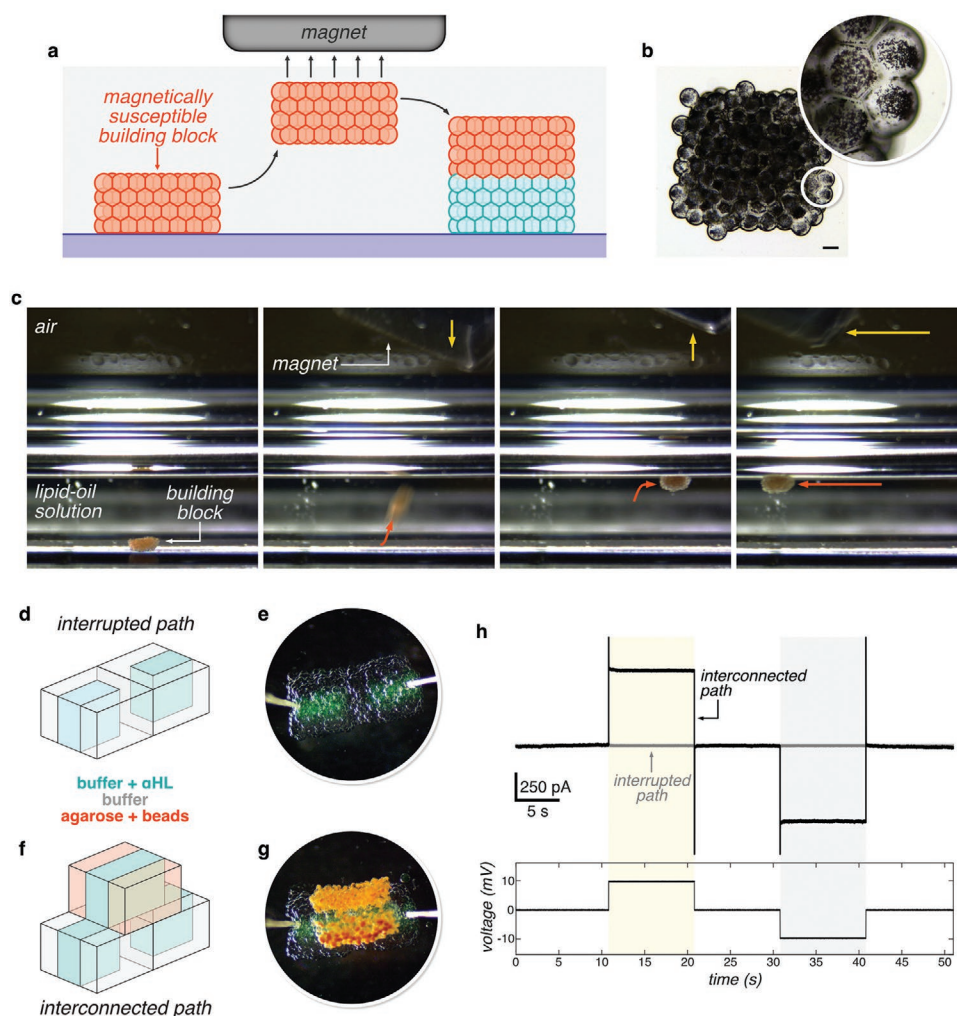


Figure 4. Stacking building blocks by magnetic levitation. a) Diagram of the stacking of building blocks by magnetic levitation. A building block containing paramagnetic beads (red) can be lifted and deposited on top of a second building block not containing beads (teal). b) Brightfield stereomicroscopy image of a 3D-printed building block containing paramagnetic beads in the droplets (black dots). To protect the bilayers during magnetic levitation, the beads are embedded within gelled agarose. Scale bar, 100 μm . c) Side-view stereomicroscopy images of the levitation of a 3D-printed building block (orange) using a neodymium magnet. Yellow and red arrows indicate the movement of the magnet and of the building block, respectively. d) Diagram of an assembled synthetic tissue containing a conductive droplet pathway (teal) interrupted by non-conductive droplets (gray). e) Top-down stereomicroscopy image of the synthetic tissue described in (d). f) Diagram of the synthetic tissue described in (d) after addition of a magnetically susceptible building block (orange) containing a conductive pathway (teal) bridging the originally interrupted pathway. g) Top-down stereomicroscopy image of the synthetic tissue described in (f). h) Electrical recordings of ionic currents flowing through the synthetic tissue before (gray trace) and after (black trace) addition of the magnetically susceptible building block bridging the originally interrupted pathway.

other as a Ca^{2+} sensor module (Figure 5a). The reservoir and sensor modules contained CaCl_2 and a membrane-impermeant Ca^{2+} indicator dye (Rhod-dextran, MW 10 kDa), respectively, and both contained wild-type αHL to allow the movement of ions. After assembly, we visualized the diffusion of Ca^{2+} ions through the droplets of the sensor module over time. A wave of fluorescence starting from the droplets located closer to the source of Ca^{2+} ions was observed, which reached the droplets at the opposite end of the sensor block within 4 h (Figure 5b; Video S2, Supporting Information).

We then used our assembly strategy to generate concentration gradients of chemicals within bacterial cultures. We assembled a hybrid tissue composed of a synthetic building block, containing a fluorescent nucleic acid stain (SYTO9),

with a biological building block, containing living cells. The biological building block contained RFP-tagged *Escherichia coli* cells printed in melted agarose as $8 \times 9 \times 5$ ($w \times d \times h$) droplets at $\approx 30^\circ\text{C}$, followed by gelling at 4°C for 1 h. We have previously shown that 3D-printed cultures of living bacteria can be generated using this methodology.^[24] After assembly, the SYTO9 released from the synthetic building block produced an increase in fluorescence of the cells in the biological building block, (Figure 5d; Video S3, Supporting Information). In this way, we visualized the localized delivery of chemical signals to living cells, demonstrating the potential of our assembly strategy to study the interaction and communication between synthetic and living systems in the future.

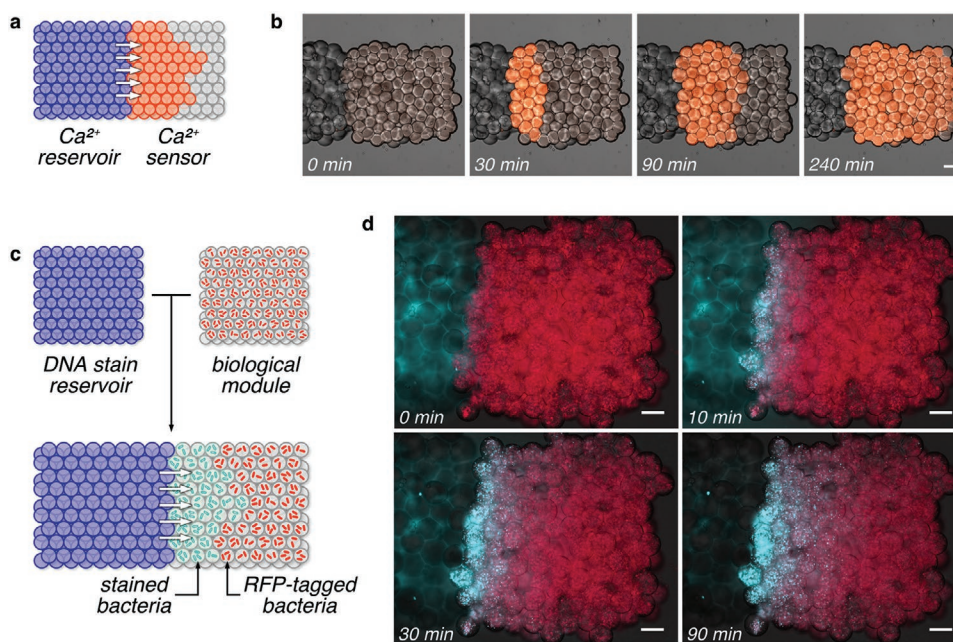


Figure 5. Diffusion of ions and molecules in synthetic and hybrid tissues. a) Diagram of an assembled synthetic tissue composed of a Ca^{2+} reservoir and a Ca^{2+} sensor module. Lipid bilayers in both modules are permeabilized with αHL . The diffusion of Ca^{2+} from the reservoir module through the sensor module is tracked by an encapsulated membrane-impermeable Ca^{2+} indicator dye (red). b) Composite brightfield and fluorescence microscopy images of the diffusion wave of Ca^{2+} throughout the sensor module, visualized by the increase in fluorescence of Rhod-dextran (MW 10 kDa) Ca^{2+} indicator dye. c) Diagram of the assembly of a hybrid tissue composed of a DNA stain reservoir (SYTO9) and a biological module encapsulating living cells (RFP-tagged *E. coli*, red). Upon assembly, the DNA stain diffuses into the biological module, staining the cells within it. d) Composite brightfield and epifluorescence microscopy images of the biological module after assembly. Encapsulated cells located closer to the reservoir module are selectively stained by the DNA stain, which binds to their DNA and increases in fluorescence (cyan).

2.6. Assembly of Modular Synthetic Tissues

Lastly, we aimed to assemble synthetic tissues that carry out logic operations. Unlike conventional solid-state logic gates that operate using electrical input signals, we integrated chemical input signals to produce electrical outputs. To this end, we used the Zn^{2+} -sensitive αHL mutant $\alpha\text{HL-4H}$, obtained by mutating residues Asn123, Thr125, Gly133, and Leu135 to histidine,^[20,25] to build modular synthetic tissues implementing the logic operations NOT and NOR. With these mutations, heptamers of $\alpha\text{HL-4H}$ allow the flow of ionic currents in the absence of Zn^{2+} ions. In the presence of Zn^{2+} ions, the pore is blocked (Figure 6a).^[25]

We first assembled synthetic tissues implementing the NOT logic operation:

$$\text{output} = \text{NOT}(\text{input}) \quad (4)$$

where the input represents the absence ($\text{input} = 0$) or presence ($\text{input} = 1$) of Zn^{2+} , and the output represents the flow of ionic current through the synthetic tissue I_{output} ($\text{output} = 0$: low/no current, $\text{output} = 1$: high current). The input module contained wild type αHL without ($\text{input} = 0$) or with ($\text{input} = 1$) Zn^{2+} , and the processing module contained $\alpha\text{HL-4H}$ (Figure 6b). Upon application of a voltage $V = 10$ mV, we measured a steady-state ionic current $I_{\text{output}} = 1.7 \pm 0.2$ nA flowing through the assembled synthetic tissue when the input module did not contain Zn^{2+} , while no current was detected when Zn^{2+} was included

as the input (Figure 6c; Table S5, Supporting Information). Therefore, through this design, we successfully implemented the NOT logic operation.

We next assembled a synthetic tissue implementing the NOR logic operation (Figure 6d):

$$\text{output} = \text{NOR}(\text{input}_1, \text{input}_2) \quad (5)$$

where the inputs represent the absence of Zn^{2+} (input_1 and $\text{input}_2 = 0$) or presence of Zn^{2+} in either or both input modules ($\text{input}_1, \text{input}_2 = \{0,1\}$ or $\{1,0\}$ or $\{1,1\}$), and output represents the flow of ionic current through the synthetic tissue I_{output} ($\text{output} = 0$: low/no current, $\text{output} = 1$: high current). Such a synthetic tissue should allow an ionic current to flow only if neither input contains Zn^{2+} , while no current flows if either input or both inputs contain Zn^{2+} .

To achieve this, two input modules encapsulating wild type αHL and without ($\text{input} = 0$) or with ($\text{input} = 1$) Zn^{2+} were connected to a rectangular processing module containing $\alpha\text{HL-4H}$ (Figure 6e) and incubated for 18 h. We detected a steady-state ionic current $I_{\text{output}} = 77 \pm 0.2$ nA only when neither input module contained Zn^{2+} . No current was detected when either input or both inputs contained Zn^{2+} (Figure 6f). According to our design, in the cases with mixed inputs ($\{0, 1\}$ or $\{1, 0\}$), Zn^{2+} ions contained in one of the input modules diffused to the other input module, blocking the $\alpha\text{HL-4H}$ pores in the whole structure (Figure 6e). We further verified this mechanism with electrical recordings of ionic currents flowing through the

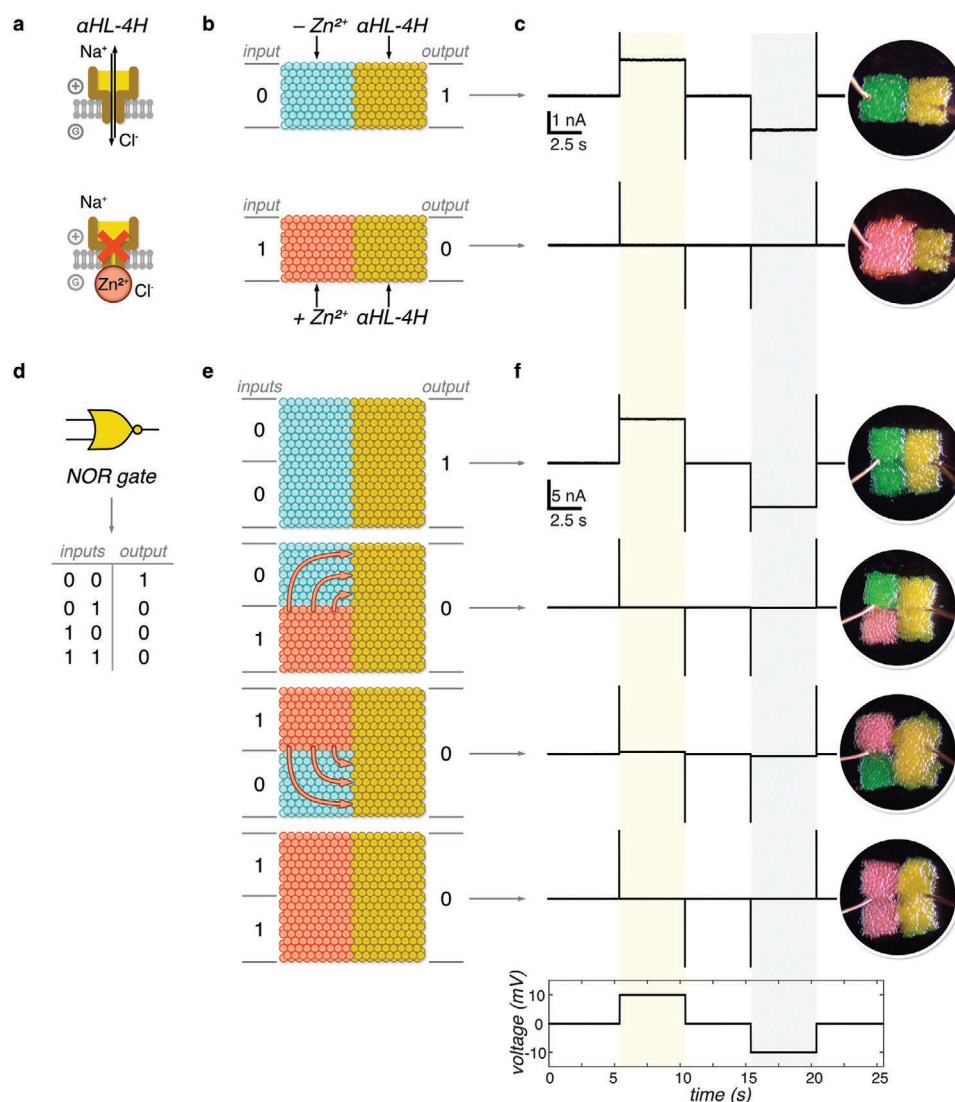


Figure 6. Modular bio-electronic devices. a) Diagram of the mechanism of the Zn²⁺-sensitive protein pore α HL-4H. In the absence of Zn²⁺, α HL-4H pores are open and ionic currents can flow. When Zn²⁺ is present, the α HL-4H pores are blocked, and no ionic current flows. b) Implementation of a NOT logic gate in a modular synthetic tissue. The input module contains α HL without Zn²⁺ (teal) or with Zn²⁺ (red), and the processing module contains α HL-4H (yellow). In the absence of Zn²⁺ (input = 0), an ionic current flows through the synthetic tissue (output = 1). Conversely, when Zn²⁺ is present (input = 1), no ionic current flows (output = 0). c) Recordings of ionic currents flowing through the synthetic tissues described in (b). Stereomicroscopy images of the corresponding synthetic tissues are shown as insets. d) Truth table for a NOR logic gate. e) Implementation of a NOR logic gate in a modular synthetic tissue. All combinations of two square input modules containing Zn²⁺ (red) or not containing Zn²⁺ (teal) are joined to a rectangular processing module (yellow). When Zn²⁺ is not present in either input (inputs = {0, 0}), an ionic current flows through the synthetic tissue (output = 1). In the cases of mixed inputs (inputs = {0, 1} and inputs = {1, 0}), Zn²⁺ can diffuse to the input module without Zn²⁺, resulting in blockage of current through the synthetic tissue (output = 0). When Zn²⁺ is present in both inputs (input = {1, 1}), no ionic current can flow (output = 0). f) Electrical recordings of ionic currents flowing through the synthetic tissues described in (e). Stereomicroscopy images of the corresponding synthetic tissues are shown as insets.

synthetic tissues, measured from each of the input modules (Figure S6, Supporting Information).

3. Conclusions

We have demonstrated the assembly of 3D-printed building blocks into higher order, modular synthetic tissues. We connected independently printed building blocks and formed func-

tional bilayers at their interfaces (Figure 2). We scaled up the production of synthetic tissues by 3D-printing building blocks in parallel (Figure 3). By these means, we assembled a synthetic tissue able to transmit an electrical signal over centimeter distances through thousands of interconnected droplets permeabilized with transmembrane protein pores. We obtained patterns in the assembled synthetic tissues by both arranging various building blocks in specific architectures, and by assembling building blocks containing printed patterns within them. We

also demonstrated the generation of magnetically susceptible building blocks by encapsulating paramagnetic beads within them, enabling contact-free manipulation and assembly in 3D (Figure 4). We visualized the diffusion of Ca^{2+} ions through αHL nanopores in synthetic tissues. Further, we assembled hybrid tissues by interfacing a synthetic building block with a biological building block containing living cells and demonstrated the localized delivery of chemicals to living cells (Figure 5). Lastly, we used the Zn^{2+} -sensitive protein nanopore $\alpha\text{HL-4H}$ to assemble modular synthetic tissues that integrate chemical input signals and produce electrical outputs, thereby implementing the logic operations NOT and NOR (Figure 6).

Our modular synthetic tissues can be built by seamlessly combining a variety of building blocks, containing aqueous solutions, molecular cargoes, wild-type and engineered membrane proteins, paramagnetic particles, hydrogels, and living cells. We demonstrated contact-free manipulation by magnetic levitation which could be used to automate and further scale up the modular assembly of synthetic tissues. Other contact-free manipulation techniques could also be investigated in the future, such as electrowetting^[26] and acoustic tweezers.^[27] With our modular approach, we have established a powerful plug-and-play platform for the fabrication of bioinspired devices that enable interactions between synthetic and living systems. For instance, by encapsulating engineered protein nanopores as well as cell-free signaling cascades, we could assemble synthetic tissues that respond to complex environmental cues. By assembling biological building blocks containing different populations of cells, we could build custom co-cultures to study multicellular interactions under controlled conditions. Building blocks containing competing strains of bacteria could be assembled in controlled architectures to study competition at the micron scale.^[24] Complex in-vitro tissue and organ models could be generated by assembling building blocks containing mammalian cells.^[28,29] Infection and disease models could be generated by interfacing building blocks containing bacteria and mammalian cells, or cancer cells with healthy cells. Synthetic building blocks could be used to control cell metabolism and tissue development within biological building blocks via spatially and temporally controlled release of chemicals. In the future, our versatile assembly platform may enable the study and design of communication pathways between synthetic and living systems, and the fabrication of advanced implants for diagnostic, therapeutic, and theranostic applications.

4. Experimental Section

Lipid-Oil Solutions: DPhPC lipids were purchased from Avanti Polar Lipids in powder form. Lipids were dissolved in chloroform (anhydrous, Sigma Aldrich) and aliquoted into isopropanol-cleaned Teflon-capped glass vials (Supelco). The chloroform was then evaporated under a slow stream of nitrogen while rotating the glass vial, to produce a lipid film at the bottom of the vial. The lipid film was then dried overnight (>16 h) under vacuum and stored under argon at -80°C . On the day of use, an oil solution composed of undecane (Sigma Aldrich) and silicone oil AR20 (Wacker) was prepared in a glass vial and added to the lipid film at room temperature. The lipid-oil solution was sonicated in a sonicator bath (Branson) for 1 h. For all experiments, the final composition of the lipid-oil solution was 2 mM DPhPC in 35:65 v:v undecane to silicone oil.

Generation of αHL and $\alpha\text{HL-4H}$ Pores: Recombinant αHL was expressed in *E. coli* and purified as previously described.^[22] In brief, $\alpha\text{HL-D8H6}$ was expressed in *E. coli* BL21(DE3)plysS cells (Agilent) and purified on Ni-NTA agarose, followed by size exclusion chromatography. Monomers were aliquoted and stored at -80°C until use.

Plasmids expressing $\alpha\text{HL-4H}$ were generated by homologous recombination. The $\alpha\text{HL-D8H6}$ plasmid was digested at the end of the $\alpha\text{HL-D8H6}$ gene using HindIII and then amplified with polymerase chain reaction (PCR) primers to generate two fragments, each of which encoded two of the required mutations. The fragments overlapped with each other as well as the upstream and downstream regions of the $\alpha\text{HL-D8H6}$ gene. The PCR conditions were as follows: 98°C for 30 s, 35 cycles of 98°C for 10 s, 55°C for 30 s, and 72°C (for the extension time specified below), and 72°C for 5 min. The extension times and PCR primers were as follows: 4H-C-FWD (5' GGTGATGATACAGGAAAAATTCACGGCCACATTG GTGCAATGTTTCG 3')^[20] and C-CT-REV (5' GCCGGATCCAAGCTTATCAATGATGGTGGTGG 3') for amplification of the C-terminal half of the αHL gene with extension time = 30 s, CT-N-FWD (5' CACCATCATTGATAAGCTTGGATCCGGCTGCTAACAAAG 3') and N-4H-REV (5' AATTTTTCTGTATCATCACCATGAACATGACCGTTGAATCCATAAG 3')^[20] for amplification of the N-terminal half of the αHL gene with extension time = 135 s.

Homologous recombination was carried out in *E. coli* XL-10 Gold cells (Agilent) thawed on ice. PCR products (0.25–0.5 μL) were added into 15 μL of cells, which were then incubated on ice for 30 min. The cells were heat-shocked at 42°C for 30 min, cooled on ice, plated onto LB-agar plates containing 100 $\mu\text{g mL}^{-1}$ ampicillin, and grown at 37°C for 16 h. Single colonies were then grown in LB containing 100 $\mu\text{g mL}^{-1}$ ampicillin for 16 h. Plasmids were purified using the PureYield plasmid miniprep system (Promega) and sequenced by Sanger sequencing, using primers S-FWD (5' CGATCCCGGAAATTAATACGACTC 3') and S-REV (5' GCTCAGCGGTGGCAGCAGC 3').

The $\alpha\text{HL-4H}$ protein was expressed by in-vitro transcription and translation (IVTT) using the PURExpress In Vitro Protein Synthesis kit (NEB, E6800) according to manufacturer's specifications, with addition of Murine RNase Inhibitor (NEB, MB0314). The plasmid containing the $\alpha\text{HL-4H}$ gene was at a final concentration of 5 $\mu\text{g mL}^{-1}$ in a reaction volume of 10 μL . Expression was carried out at 37°C for 3 h, after which the PURExpress reaction mix was diluted for 3D-printing.

Culture of Bacteria and Bioink Preparation: Cultures of chromosomally labelled mRFP1 BZB1011 *E. coli* strains (RFP-tagged *E. coli*) were started directly from glycerol stocks in 4 mL LB medium and shaken at 250 rpm for 16 h overnight at 37°C . A portion of the culture (40 μL) was added to fresh LB medium (4 mL) and cultured for 3 h at 37°C with shaking at 250 rpm. The cells were then recovered by centrifugation at 8000 rcf for 5 min and resuspended at 10^{10} cells/mL in melted 1.5% w/v ultra-low gelling temperature agarose in M9 medium (at 37°C).

Aqueous Solutions: All aqueous solutions in the experiments shown in Figures 1 and 2 were composed of 25 mM Tris-HCl pH 7.6 (Sigma Aldrich), 1 M NaCl (Sigma Aldrich) and 0.1% w/v Pluronic F68. In the droplets forming the conductive pathways, 30 $\mu\text{g mL}^{-1}$ αHL and 10 μM of a water-soluble fluorescent dye (Atto488 or Atto565 for green or red droplets, respectively, Sigma Aldrich) were also added. For experiments shown in Figure 3, the magnetically susceptible droplets were composed of 25 mM Tris-HCl pH 7.6, 1 M NaCl, 1.5% w/v ultra-low gelling temperature agarose (Sigma Aldrich), and 7.75 mg mL^{-1} paramagnetic beads (Dynabeads MyOne Carboxylic Acid, diameter 10 μm , Thermo Fisher Scientific). For experiments shown in Figure 4, the input modules contained 25 mM Tris-HCl pH 7.6, 1 M NaCl (input = 0) or 0.85 M NaCl, and 0.1 M ZnCl_2 (input = 1), with 0.1% (w/v) Pluronic F68, 5 mM EDTA (Sigma Aldrich), and 30 $\mu\text{g mL}^{-1}$ αHL . The processing blocks were composed of 25 mM Tris-HCl pH 7.6, 1 M NaCl, 0.1% (w/v) Pluronic F68, 5 mM EDTA, and 5% v/v PURExpress mix in which $\alpha\text{HL-4H}$ had been expressed. For experiments shown in Figure 6b, the Ca^{2+} reservoir building block was composed of 25 mM Tris-HCl pH 7.6, 0.67 M CaCl_2 (Sigma Aldrich), 0.1% (w/v) Pluronic F68, 25 mM dextran (MW 10 000, Sigma Aldrich), 10 mM EDTA, and 50 $\mu\text{g mL}^{-1}$ αHL . The Ca^{2+} sensor

building block was composed of 25 mM Tris-HCl pH 7.6, 1 M NaCl, 0.1% (w/v) Pluronic F68, 25 mM Rhod-dextran (MW 10 000, Thermo Fisher Scientific), 10 mM EDTA, and 50 $\mu\text{g mL}^{-1}$ αHL . The addition of 0.1% w/v Pluronic F68 in the solutions described above aided with the solubilization of hydrophobic or amphiphilic components of the aqueous solutions (e.g., αHL , hydrophobic components of the PURExpress mix) and stabilization of the lipid bilayers. For experiments shown in Figure 6d, the reservoir building block contained 100 μM SYTO 9 (Thermo Fisher Scientific) in M9 medium, while the biological building block contained RFP-tagged *E. coli* cells at a concentration of 10^{10} cells/mL and 1.5% (w/v) ultra-low gelling temperature agarose in M9 medium.

3D-Printing Building Blocks: 3D-printed building blocks were generated as previously described.^[8,16] In brief, droplet networks were formed by 3D-printing picoliter-sized aqueous droplets (diameter 100 μm , volume ≈ 520 pL) into a lipid-oil bath contained within a glass or PMMA container on a micromanipulator stage. Ejection of the droplets was driven by the actuation of a piezo-electric transducer which generates controlled pressure pulses inside a glass nozzle filled with Milli-Q water (Millipore). The glass nozzle consisted of a pulled glass capillary with tip diameter of ≈ 100 μm , from which the aqueous ink was ejected. An undecane oil plug (≈ 5 μL) separated the aqueous ink solution from the water in the nozzle. The placement of the droplets was controlled by synchronizing the motion of the micromanipulator stage (PatchStar micromanipulator, Scientifica) with the droplet ejection, using custom software (LabView). When possible, building blocks were 3D-printed in parallel by synchronizing the ejection of two printing nozzles within the same printing container. For the experiments shown in Figure 3f,g, patterned building blocks were obtained by synchronizing the movement of the stage and the ejection of two types of droplets from two nozzles to form an L-shaped pattern. Building blocks containing agarose were 3D-printed at ≈ 30 $^{\circ}\text{C}$ by using an IR heater (Beurer Ltd.), as previously described.^[24] After printing, the building blocks containing agarose were gelled at 4 $^{\circ}\text{C}$ for 1 h.

Assembly of Synthetic Tissues: With the exception of the experiments shown in Figure 4, the 3D-printed building blocks were manipulated and assembled by hand using a flat metal spatula. To connect two building blocks, one of the building blocks was put in contact with the other using the spatula, and a gentle pressure was then applied for ≈ 20 – 30 s to ensure the formation of lipid bilayers at the contact interface. For the experiments shown in Figure 4, magnetically susceptible building blocks were levitated within the lipid-oil bath using a neodymium magnet, as shown in Video S1, Supporting Information.

Electrical Recordings: Electrical recordings on the assembled synthetic tissues were performed as previously described.^[16] In brief, the recordings were performed inside a Faraday cage (Mechanical Workshop, University of Oxford) using a patch-clamp amplifier (Axopatch 200B, Axon Instruments). The electrodes were silver wires (100 μm diameter), which had been incubated in sodium hypochlorite solution (Sigma Aldrich) for 15 min and subsequently coated with a thin layer of 1.5% w/v ultra-low gelling temperature agarose in the same buffer solution contained within the assembled synthetic tissues. The electrodes were manipulated and connected to the synthetic tissues using two micromanipulators (Narishige, NMN-1). The electrical traces were recorded using pClamp 10 (Molecular Devices) software and were analyzed using MATLAB.

Imaging of Synthetic Tissues: The assembled synthetic tissues were imaged during electrical recordings using an AmScope MU1000A digital camera fitted on the ocular of a Nikon SMZ645 stereomicroscope. A warm white LED was used as a light source (Thorlabs, MWHL1P LED through COPI-A collimator and powered by LEDD1B driver). Confocal images were acquired using a Leica SP5 laser scanning confocal microscope. Epi-fluorescence images were acquired using a Leica DMI8 inverted epi-fluorescence microscope.

Statistical Analysis: All shown electrical traces were acquired at a sampling frequency of 10 kHz, filtered at 2 kHz with 0.5X gain. Throughout the text, the current levels were presented as mean \pm SD, calculated over $n = 100\ 000$ (Figures 2–4) or $n = 50\ 000$ (Figure 5)

samples. The analysis of the current traces was performed in MATLAB using a custom script.

Supporting Information

Supporting Information is available from the Wiley Online Library or from the author.

Acknowledgements

This research was funded by a European Research Council Advanced Grant (grant ERC-2018-ADG). A.A. and I.C. acknowledge funding from the University of Oxford, the EPSRC & BBSRC Centre for Doctoral Training in Synthetic Biology (grant EP/L016494/1) and the Clarendon Fund Scholarship. A.A. acknowledges funding from the Cyril & Phillis Long Studentship. I.C. acknowledges funding from the Oxford-Broomhead Graduate Scholarship.

Conflict of Interest

The authors declare no conflict of interest.

Data Availability Statement

The data that support the findings of this study are openly available in Figshare at <http://doi.org/10.6084/m9.figshare.16811860>, reference number [30].

Keywords

bioinspired materials, nanopores, synthetic biology, synthetic tissues

Received: August 28, 2021

Revised: October 6, 2021

Published online: November 5, 2021

- [1] C. Y. Baldwin, K. B. Clark, *Design Rules: The Power of Modularity*, The MIT Press, Cambridge, MA, USA 2000.
- [2] K. Ulrich, K. Tung, *In American Society of Mechanical Engineers, Design Engineering Division*, ASME, 1991, p. 73, https://link.springer.com/chapter/10.1007/978-94-011-1390-8_12.
- [3] M. Pigliucci, *Nat. Rev. Genet.* **2008**, 9, 75.
- [4] J. Clune, J. B. Mouret, H. Lipson, *Proc. R. Soc. B* **2013**, 280, 20122863.
- [5] S. Tasoglu, E. Diller, S. Guven, M. Sitti, U. Demirci, *Nat. Commun.* **2014**, 5, 3124.
- [6] H. Qi, M. Ghodousi, Y. Du, C. Grun, H. Bae, P. Yin, A. Khademhosseini, *Nat. Commun.* **2013**, 4, 2275.
- [7] R. Subbiah, C. Hipfinger, A. Tahayeri, A. Athirasala, S. Horsophonphong, G. Thirvikraman, C. M. França, D. A. Cunha, A. Mansoorifar, A. Zahariev, J. M. Jones, P. G. Coelho, L. Witek, H. Xie, R. E. Guldberg, L. E. Bertassoni, *Adv. Mater.* **2020**, 32, 2001736.
- [8] G. Villar, A. D. Graham, H. Bayley, *Science* **2013**, 340, 48.
- [9] P. Gobbo, A. J. Patil, M. Li, R. Harniman, W. H. Briscoe, S. Mann, *Nat. Mater.* **2018**, 17, 1145.
- [10] D. T. Gonzales, C. Zechner, T. Y. D. Tang, *Curr. Opin. Syst. Biol.* **2020**, 24, 56.

- [11] M. A. Holden, D. Needham, H. Bayley, *J. Am. Chem. Soc.* **2007**, *129*, 8650.
- [12] H. Bayley, I. Cazimoglu, C. E. G. Hoskin, *Emerging Top. Life Sci.* **2019**, *3*, 615.
- [13] G. Villar, A. J. Heron, H. Bayley, *Nat. Nanotechnol.* **2011**, *6*, 803.
- [14] A. Alcinesio, R. K. Kumar, H. Bayley, *ChemSystemsChem* **2021**, *3*, e2100036.
- [15] G. Maglia, A. J. Heron, W. L. Hwang, M. A. Holden, E. Mikhailova, Q. Li, S. Cheley, H. Bayley, *Nat. Nanotechnol.* **2009**, *4*, 437.
- [16] A. Alcinesio, O. J. Meacock, R. G. Allan, C. Monico, V. R. Schild, I. Cazimoglu, M. T. Cornall, R. K. Kumar, H. Bayley, *Nat. Commun.* **2020**, *11*, 2105.
- [17] M. J. Booth, V. R. Schild, A. D. Graham, S. N. Olof, H. Bayley, *Sci. Adv.* **2016**, *2*, e1600056.
- [18] L. D. Hughes, R. J. Rawle, S. G. Boxer, *PLoS One* **2014**, *9*, e87649.
- [19] T. Wauer, H. Gerlach, S. Mantri, J. Hill, H. Bayley, K. T. Sapra, *ACS Nano* **2014**, *8*, 771.
- [20] M. J. Booth, I. Cazimoglu, H. Bayley, *Commun. Chem.* **2019**, *2*, 142.
- [21] A. Dupin, F. C. Simmel, *Nat. Chem.* **2019**, *11*, 32.
- [22] I. Cazimoglu, M. J. Booth, H. Bayley, *bioRxiv* **2021**, 2021.05.05.442835.
- [23] P. G. Slade, *Electrical Contacts: Principles and Applications*, Second Edition, CRC Press, Boca Raton, FL, USA **2017**.
- [24] R. K. Kumar, T. A. Meiller-Legrand, A. Alcinesio, D. Gonzalez, D. A. I. Mavridou, O. J. Meacock, W. P. J. Smith, L. Zhou, W. Kim, G. S. Pulcu, H. Bayley, K. R. Foster, *Nat. Commun.* **2021**, *12*, 857.
- [25] O. Braha, B. Walker, S. Cheley, J. J. Kasianowicz, L. Song, J. E. Gouaux, H. Bayley, *Chem. Biol.* **1997**, *4*, 497.
- [26] M.-Y. Chiang, Y.-W. Hsu, H.-Y. Hsieh, S.-Y. Chen, S.-K. Fan, *Sci. Adv.* **2016**, *2*, e1600964.
- [27] A. Ozcelik, J. Rufo, F. Guo, Y. Gu, P. Li, J. Lata, T. J. Huang, *Nat. Methods* **2018**, *15*, 1021.
- [28] A. D. Graham, S. N. Olof, M. J. Burke, J. P. K. Armstrong, E. A. Mikhailova, J. G. Nicholson, S. J. Box, F. G. Szele, A. W. Perriman, H. Bayley, *Sci. Rep.* **2017**, *7*, 7004.
- [29] L. Zhou, A. C. Wolfes, Y. Li, D. C. W. Chan, H. Ko, F. G. Szele, H. Bayley, *Adv. Mater.* **2020**, *32*, 2002183.
- [30] A. Alcinesio, H. Bayley, Modular Synthetic Tissues from 3D-Printed Building Blocks: Raw Data; Figshare, **2021**, <http://doi.org/10.6084/m9.figshare.16811860>.